Received 10 October 2023; revised 22 November 2023; accepted 12 December 2023. Date of publication 19 December 2023;
date of current version 11 January 2024.

Digital Object Identifier 10.1109/OJCOMS.2023.3344411

Modulations for Terahertz Band Communications: Joint Analysis of Phase Noise Impact and PAPR Effects

CLAIRE T. PARISI [1] (Member, IEEE), SHERIF BADRAN [2] (Graduate Student Member, IEEE), PRIYANGSHU SEN [3] (Member, IEEE), VITALY PETROV [2] (Member, IEEE), AND JOSEP MIQUEL JORNET [2] (Fellow, IEEE)

[1]Air Force Research Laboratory, Rome, NY 13441, USA

[2]Department of Electrical and Computer Engineering, Northeastern University, Boston, MA 02115, USA

[3]Department of Engineering, SUNY Polytechnic Institute, Utica, NY 13502, USA

CORRESPONDING AUTHOR: C. T. PARISI (e-mail: claire.parisi@us.af.mil)

This work was supported in part by the National Science Foundation under Award CNS-1955004, Award CNS-2011411, and Award CNS-2225590; and in part by the Air Force Research Laboratory under Award FA8750-20-1-02000.

ABSTRACT The choice of modulation techniques for next-generation communications in the sub-terahertz and terahertz bands remains largely unresolved. A variety of traditional and new schemes show promise, but the question remains open on the illustrative comparison process for realistic terahertz systems. While there are some preliminary studies in this area, we emphasize that the peculiarities of terahertz hardware necessitate a scheme that (i) is resistant to system-wide phase noise (PN) and (ii) has a low peak-to-average power ratio (PAPR). Therefore, in this article, we present a comprehensive methodology to carefully model and jointly study the impacts of PN and PAPR on the performance of candidate modulations for terahertz links. We first deliver a mathematical model for sub-terahertz/terahertz phase noise impairments at 130 GHz, 225 GHz, and 1.02 THz based on measurements from actual terahertz hardware. We then introduce the *PAPR penalty* – an approach for fair comparison of bit error rate (BER) and spectral efficiency (SE) of modulation schemes with different PAPRs. We finally combine these two effects to comprehensively study the characteristics of single and multi-carrier modulation schemes for terahertz communications. Our study reveals that analyzing PAPR and PN jointly is paramount: accounting for only one leads to major deviations in the numerical results and misleading conclusions on best modulation choice(s). The delivered framework and evaluation should facilitate further studies, leading to a well-motivated selection of the most suitable modulation scheme(s) for prospective sub-terahertz and terahertz radio systems.

INDEX TERMS Digital modulation, OFDM, OTFS, PAPR, phase noise, terahertz communications.

I. INTRODUCTION

LOOKING ahead to 6G/7G communications, it is projected that systems will continue to migrate to higher frequencies, namely, the sub-terahertz (100 GHz–300 GHz) and terahertz (300 GHz–3 THz) bands. These bands promise larger contiguous swaths of bandwidth and higher data rates, eventually supporting terabit-per-second links [1], [2], [3], [4]. The faster communications enabled by the terahertz band will be essential to the development of new technologies and use cases in a variety of applications including, but not limited to, health, military, and entertainment [5], [6], [7].

Choosing the appropriate modulation technique(s) is fundamental when adopting new frequency bands for communications. While many existing modulation schemes have already been comprehensively evaluated at lower frequencies, terahertz systems come with their own set of

unique challenges [8], motivating the analysis of modulation schemes and their performance trade-offs with respect to the terahertz-specific peculiarities and limitations. There are numerous good articles modeling and analyzing the terahertz channel properties for communications. For example, theoretical and simulation-based studies, including [7], [9], [10], [11], [12], [13], [14], [15], among many others, show that a variety of scenarios and applications for terahertz communications must be considered, as the terahertz channel is notably different among them. This is further corroborated by the extensive measurement campaigns conducted in [1], [12], [14], [16], [17], [18] and many other studies, which show different results depending on the environment. Complementing the mainly channel-centric studies above, in this article, we focus primarily on hardware effects, specifically, phase noise (PN) and peak-to-average power ratio (PAPR). Both appear to be important for terahertz communications but are often overlooked in pure channel-centric studies when evaluating the performance of terahertz wireless systems in different scenarios.

Modern terahertz hardware suffers from several impairments. Practical systems exhibit frequency-selectivity and non-linearity [19], [20], which cause distortions in the transmitted signals. Pre-distortion techniques are well studied [21], [22] and can help compensate for this effect. High PN is also observed in terahertz hardware [23] attributed to noise in the active components of local oscillators (LOs) as well as within frequency multipliers. While a phase-locked loop can mitigate this effect, it significantly adds to the overall system complexity. Additionally, even state-of-the-art power amplifiers have limitations and are sensitive to intense fluctuations in power levels [24]. Over-saturation of the amplifier can lead to non-linear distortions or even equipment damage, limiting the transmit power. With this, the PAPR of a signal becomes an important metric as signals with a lower PAPR can be transmitted at a higher power.

Along with the challenges of terahertz systems, signals at these frequencies will be much different than sub-6 GHz systems: larger spectrum availability ultimately means that signals will occupy more bandwidth, with multi-GHz bandwidth [25]. Because of these factors, we must evaluate the physical layer design choices for terahertz systems and select modulation methods that not only enable high data rates required for 6G/7G applications but also meet the demands of terahertz system considerations. In this work, we focus on considerations related to hardware impairments (resistance to PN and inherently low PAPR). We show how each effect on its own contributes significantly to performance. We also demonstrate the importance of joint evaluation, providing a method for analyzing modulation schemes for their suitability with terahertz-band systems.

A. RELATED WORKS ON MODULATION SCHEMES FOR TERAHERTZ

Many modulation schemes have been proposed and evaluated for use in higher bands. Current 4G and 5G New Radio (5G NR) systems rely mainly on Orthogonal Frequency Division Multiplexing (OFDM) because of its robustness to frequency selectivity and spectral efficiency (SE). While it is shown that OFDM can be adapted for terahertz-band systems [26], its performance is non-ideal in certain regimes [27] (as also further illustrated in the article). Therefore, many researchers are looking into alternatives and variations on OFDM as potential better candidates for terahertz systems. In [28] single versus multi-carrier candidates are introduced for use in the terahertz band including OFDM, Discrete Fourier Transform-Spread-Orthogonal Frequency Division Multiplexing (DFT-s-OFDM), Orthogonal Time Frequency Space (OTFS), Discrete Fourier Transform-Spread-Orthogonal Time Frequency Space (DFT-s-OTFS), as well as Universal Filtered Multi-Carrier (UFMC), Filter-Bank Multi-Carrier (FBMC), and Generalized Frequency Division Multiplexing (GFDM).

DFT-s-OFDM and OTFS have emerged as popular alternatives to OFDM. DFT-s-OFDM is a single-carrier take on OFDM that inserts a pre and post-processing discrete Fourier transform (DFT) block into OFDM [29]. DFT-spreading has become a popular choice for reducing the PAPR of OFDM with many variations proposed including generalized, zero-tail, zero-word, enhanced, guard-interval, and unique-word DFT-s-OFDM [30], [31], [32], [33], [34], [35], all with their own set of advantages and disadvantages. Applying DFT-spreading to other schemes, like OTFS is also proposed with promising results for bit error rate (BER) improvement and PAPR reduction [36], [37]. For this work, we focus only on DFT-s-OFDM. On the other hand, OTFS has garnished attention for next-generation modulation [38], its use of the delay-Doppler domain for high-mobility applications [39], and better performance in PN [40].

In addition, traditional techniques like spread spectrum are proposed to both exploit the large available bandwidth at terahertz frequencies and enable covert communications that are harder to detect [41]. Recently, two different approaches to spread-spectrum communications at sub-terahertz frequencies have been designed and experimentally demonstrated, namely, direct-sequence spread spectrum (DSSS), aimed at facilitating coexistence between active and passive users of the spectrum [42], and chirp spread spectrum communications, which enhanced robustness against narrow-band absorption and interference [43]. Additional work has also been done on constellations for single-carrier schemes for terahertz frequencies. For example, most of the long-range experimental works rely on phase-only modulations (e.g., phase-shift keying (PSK) [44]), or conventional quadrature amplitude modulation (QAM) (e.g., [45]). In addition, to precisely reduce the PAPR of QAM modulations, carefully designed amplitude and phase-shift keying (APSK), which encode the information in symbols across multiple concentric rings, have been optimized [46] and are now part of the sole existing standard for terahertz communications [47]. Still in the realm of single-carrier modulations, hierarchical bandwidth modulations and bandwidth-aware evolution of

concatenated or hierarchical modulations have been proposed as a way to encode multiple bit-streams for different users along the same direction, leveraging molecular absorption as in-channel spatial filter [48].

Complementing the works advocating for one or two solutions, several studies on evaluating the suitability of various modulation schemes for terahertz radios have recently appeared. Among others, Taraboush et al. [28] extensively analyzed each scheme regarding a variety of parameters such as PAPR, out-of-band emissions, spectral efficiency, and complexity. However, the study focuses on evaluating the parameters individually while, in real terahertz hardware, the effects come jointly. Similarly, [49] evaluates single-carrier modulation schemes in the presence of varying PN levels and delivers the key performance indicators, such as error vector magnitude (EVM) and BER among others. This is an important work, but it only studies the effects individually and utilizes a simplistic PN model not tailored to the specifics of real terahertz hardware. There are other works on the suitability of different terahertz modulation schemes in different contexts (e.g., [50] and [51], among others), however, to the best of our knowledge, our work is the first of its kind to provide a joint analysis of the effects of PN *and* PAPR effects based on practical system observations.

B. NOVELTY AND CONTRIBUTION

In our work, we deliver an evaluation framework to analyze the joint impact of terahertz hardware peculiarities on the performance of different modulation schemes. We start with properly modeling the PN and then examine the implications of higher and lower PAPR characteristics. We finally evaluate the two effects combined to understand what techniques are applicable for use in the terahertz band.

There are two major *novelties* of this work. First, as discussed above, the prior studies on modulations for terahertz primarily rely on simplistic linear PN models, as there is no comprehensive PN model tailored to sub-terahertz and terahertz radio. For instance, the widely adopted 3GPP PN models described in [52] and [53] are only valid for up to 71 GHz. We address this issue in the present manuscript by a combination of field measurements using real sub-terahertz and terahertz hardware with numerical modeling efforts. We use the measured phase noise characteristics to tailor the parameters of one of the agreed 3GPP models in [53] (specifically, the one proposed by Samsung in [54]) to match the characteristics of real sub-terahertz systems.

Second, while most of the prior studies talk about both PAPR and PN, they typically analyze them separately with different methodologies. While this information is useful, modulation choice remains difficult; performance tradeoffs arise when evaluating modulations under the lens of one design consideration at a time, so the answer remains obfuscated by the lack of a synthesized analysis. In this study, we propose a constructive method to account for both the PAPR and PN resistance within a single evaluation by exploiting the power reduction due to high PAPR as a *PAPR penalty*, as further detailed in the article. The delivered models and methodology to jointly capture the effects of PN and PAPR in terahertz systems can be partially reused in follow-up studies focused on other important aspects, including terahertz beamforming and terahertz hardware design, among others.

The key contributions of this article are thus:

- Utilizing the real hardware measurement data, we introduce phase noise models specific for the terahertz hardware operating at 130 GHz, 225 GHz, and 1.02 THz. The models stem from those adopted by the 3GPP but are better tailored to the characteristics of terahertz band equipment.
- We introduce an evaluation framework to study the characteristics of a terahertz communication system when *jointly* accounting for the effects of PN and PAPR.
- We apply the developed framework to numerically characterize the performance of a terahertz communication system with various modulation schemes, identifying the promising choices for different configurations.

The remainder of this paper is organized as follows: We discuss each candidate modulation technique in Section II. In Section III we describe PN, existing models, our measurements, and our proposed model parameters. In Section IV, we introduce PAPR limitations and describe our performance penalty for signals with high PAPR. Further, we present the numerical results of each signal in the presence of PN, PAPR, and both PN and PAPR combined in Section V. Lastly, we summarize and conclude the paper in Section VI.

II. MODULATION CANDIDATES FOR TERAHERTZ

Several candidate modulations, both single and multi-carrier, are under consideration for prospective terahertz communication systems. In this work, we will evaluate a subset of the most popular techniques. For single-carrier modulations, we assess basic techniques including QAM, PSK, and APSK. These schemes are fundamental digital communication schemes to modulate the information, where APSK is well known for low PAPR while having high spectral efficiency [46].

In addition, we consider DSSS, and DFT-s-OFDM as other single-carrier techniques. For multi-carrier systems, OFDM is naturally a contender for terahertz-band communications, in addition to exploring newer schemes, in particular, OTFS. We provide block diagrams for each in Fig. 1. Therein, for simulation, we consider the baseband equivalent of the corresponding radio frequency bandpass signal in the terahertz band with the respective amplitude and PN. Furthermore, we focus on the hardware impacts and omit the channel effects, as these drastically change with the scenario, i.e., from a crystal-clear line-of-sight channel in an absorption-defined window to a frequency-selective channel due to multipath propagation or proximity to absorption lines. Additionally, the functional blocks required for practical transmission such as up and down-conversion, pre and post-processing, addition

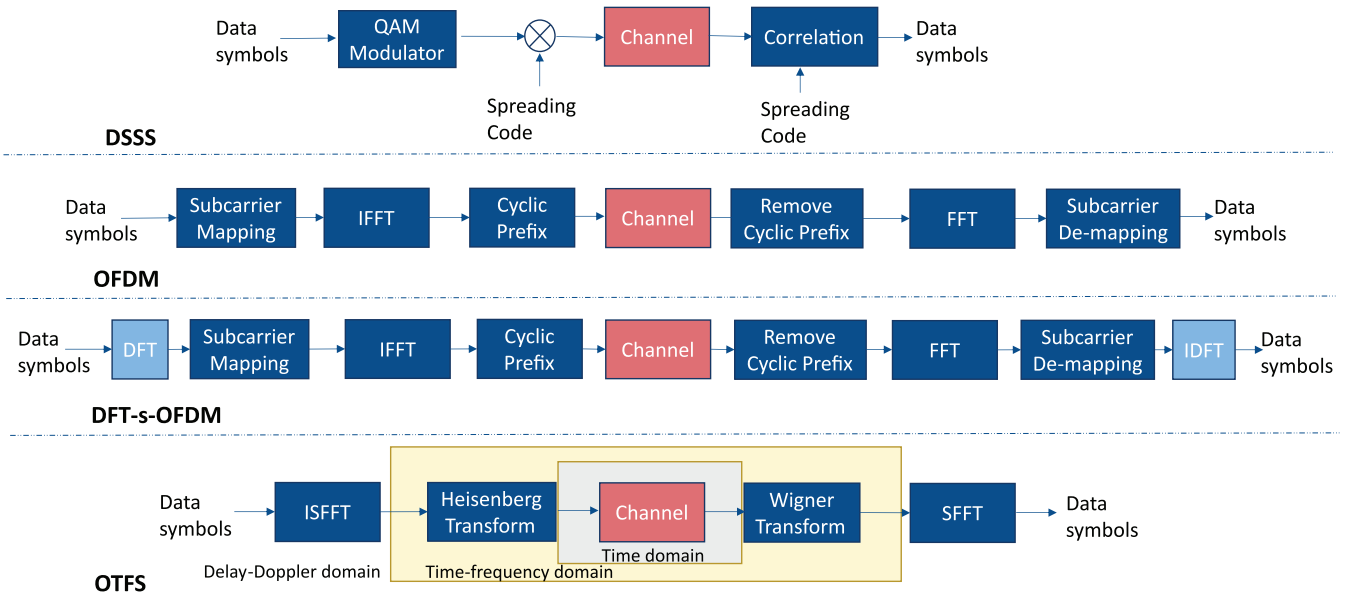

FIGURE 1. System block diagrams of DSSS, OFDM, DFT-s-OFDM, and OTFS.

of pilots, and equalization are omitted for clarity purposes. Each of these modulation schemes has specific advantages and drawbacks, which makes it difficult to determine the best candidate for terahertz communications. In the remainder of this section, we briefly describe the key elements of each of the aforementioned schemes.

A. PSK, QAM, AND APSK

PSK, QAM, and APSK are digital modulation processes that convey data by changing either the phase or both the amplitude and phase of the carrier wave. With PSK, only the phase is modified to represent a different symbol. This results in a constellation that consists of uniform angular spacing between points. The simplest cases of this are binary phase-shift keying (BPSK) and quadrature phase-shift keying (QPSK). Because there is no change in amplitude, all of the symbols are transmitted with the same energy, meaning PSK signals will not have PAPR implications. For QAM and APSK, both amplitude and phase changes indicate a new symbol. QAM has a rectangular grid of equal vertical and horizontal spacing between each point. In APSK, the constellation grid is different concentric circles with equal spacing between points in each ring and flexibility for the number of rings and symbols in each ring. Therefore, for a given value of modulation order, M, M-QAM, and M-APSK possess higher PAPR in contrast to M-PSK schemes. However, both M-QAM and M-APSK have a lower BER compared to PSK in additive white Gaussian noise (AWGN) channels due to the higher spacing between constellation points. Further, for APSK, we can trade off error performance with PAPR by choosing the number of rings within the constellation [46].

B. DSSS

In DSSS, modulated data is multiplied or spread with a known, pseudo-random spreading sequence of ± 1s. This deliberately increases the bandwidth of the signal and results in a noise-like transmission. This approach is commonly used in low probability of intercept (LPI) communications – when the information is "de-spread" via correlation of the spreading sequence at the receiver, the information is restored while interference is reduced. Fig. 1 features the block diagram for a DSSS system. In our work, we use maximum length sequences (MLSs) as our spreading codes. MLS sequences are binary pseudo-random codes that are generated by maximal linear-feedback shift registers (LFSRs). The length of the spreading sequence affects the spectral efficiency of the signal: for the same bandwidth, more spreading of the original signal means the data is sent at a slower data rate, thus reducing spectral efficiency.

C. OFDM

OFDM is a very popular modulation method utilized in 4G and 5G communications. Modulated symbols are assigned to orthogonal sub-carriers and transmitted simultaneously. Because of this, OFDM is usually robust in frequency-selective environments and has decisive spectral efficiency. At the same time, its PAPR is high as well due to the use of the inverse fast Fourier transform (IFFT) operations; linear combinations of many QAM symbols involved in the IFFT operation can create large and highly varying peaks in the output signal [55]. The block diagram in Fig. 1 shows how symbols are assigned to each sub-carrier and changed into the time-domain symbols using the IFFT,

$$x(t) = \frac{1}{N} \sum_{k=0}^{N-1} X(k)\, e^{j2\pi tk/N}, \tag{1}$$

where $x(t)$ are time domain samples, $X(k)$ are frequency domain signals, and N is the number of subcarriers.

The addition of a cyclic prefix or guard interval helps reduce inter-symbol interference by adding a buffer zone

in each OFDM symbol that is a repetition of a certain percentage of the data appended to the symbol. The length of the cyclic prefix can be adjusted depending on the channel conditions: a more severe channel calls for a longer cyclic prefix (increased overhead). For our evaluation, we set the cyclic prefix size to 5% of the symbol size; complete removal of the cyclic prefix hinders performance while a reduced size has minimal degradation as demonstrated in [26]. To recover, the steps occur in reverse: the cyclic prefix is removed, then the fast Fourier transform (FFT) is performed and the payload symbols get recovered.

D. DFT-S-OFDM

DFT-s-OFDM essentially adds an extra DFT pre/post-processing block to OFDM systems, as shown in Fig. 1. In contrast to OFDM, the precoding leads to a single-carrier transmit signal. The sequence of bits transmitted is mapped to a complex constellation (like QAM, QPSK, APSK), which is then passed through a DFT block. The DFT size must be less than the number of OFDM subcarriers [29]. From here, the output is mapped to different OFDM subcarriers and passed through an N-point IFFT, before adding a cyclic prefix and sending it through the channel. Due to the "single-carrier nature" of the DFT-s-OFDM, its PAPR also gets reduced compared to a pure OFDM. However, this comes with the trade-off of reduced spectral efficiency. DFT-s-OFDM is used in 4G-LTE/5G-NR uplink.

E. OTFS

Designed with high-mobility scenarios in mind, in OTFS, symbols are considered in the delay-Doppler domain, rather than the time-frequency domain. In the OTFS transform, two main steps occur: (i) the inverse symplectic finite Fourier transform (ISFFT) followed by (ii) the Heisenberg transform, which forms the time domain signal [56]. Starting with the $M \times N$ grid of modulated symbols in the delay-Doppler domain with entries $X[m, n]$, for $m = 0, \ldots, M-1$ and $n = 0, \ldots, N-1$, the ISFFT given by

$$X_{tf}[l, k] = \frac{1}{\sqrt{NM}} \sum_{n=0}^{N-1} \sum_{m=0}^{M-1} X[m, n]\, e^{j2\pi \left(\frac{nk}{N} - \frac{ml}{M}\right)} \tag{2}$$

converts the symbols into NM time-frequency domain samples, $X_{tf}[l, k]$ for $l = 0, \ldots, M-1$ and $k = 0, \ldots, N-1$. Essentially, the ISFFT is a 2D transformation that takes the DFT of the columns of X and an inverse discrete Fourier transform (IDFT) of the rows. From here, the Heisenberg transform is applied to get the transmit signal, $s(t)$, so that

$$s(t) = \sum_{k=0}^{N-1} \sum_{l=0}^{M-1} X_{tf}[l, k]\, e^{j2\pi l \Delta f (t - kT)}, \tag{3}$$

where Δf is the spectrum spacing which is equal to the bandwidth divided by the M number of subcarriers/delay bins, B/M and T is the block duration. The delay and Doppler bin sizes can be chosen strategically based on channel characteristics.

At the receiver, the Wigner transform forms the time-frequency domain received samples, Y_{tf}, by essentially match-filtering and sampling the points. This is followed by the symplectic finite Fourier transform (SFFT),

$$Y[m, n] = \frac{1}{\sqrt{NM}} \sum_{k=0}^{l-1} \sum_{m=0}^{M-1} Y_{tf}[l, k]\, e^{-j2\pi \left(\frac{nk}{N} - \frac{ml}{M}\right)}, \tag{4}$$

which translates the time domain signal back to the delay-Doppler domain, where the symbols, $Y[m, n]$ are decoded. Because the symbols are mapped to a delay-Doppler grid, it is more robust in high-Doppler channels with multipath [56].

III. PHASE NOISE MEASUREMENTS AND MODELING

In this section, we develop our terahertz-specific PN model. We first recall the 3GPP PN model from [54] for millimeter wave frequencies that we used as a basis. We then describe our measurement campaign to characterize the PN of a real sub-terahertz platform at different frequencies and our measurement results. We finally show how to tailor the 3GPP model parameters in a way that best fits the performance of real hardware operating in sub-terahertz and terahertz bands.

A. 3GPP PHASE NOISE MODEL

Noise from active components and lossy elements can cause leakage around the center frequency which we call PN, causing potentially significant distortion in the signal. 3GPP recommends using the multi-pole/zero model,

$$S(f) = \text{PSD0} \prod_{n=1}^{N} \frac{1 + \left(\frac{f}{f_{z,n}}\right)^2}{1 + \left(\frac{f}{f_{p,n}}\right)^2}, \tag{5}$$

to represent PN in a system [54]. $S(f)$ is the power spectral density (PSD) in dBc/Hz, PSD0 is the power spectral density at the zero-offset/frequency of interest, while $f_{z,n}$ and $f_{p,n}$ are zero and pole frequencies, respectively. PSD0 is recorded in dBc/Hz, where dBc represents the power ratio to a carrier signal, and so dBc/Hz is the power at a given frequency offset from the carrier. While this model is specific for oscillator PN, we can still utilize its framework for modeling end-to-end PN seen in practical terahertz hardware. In [53], 3GPP also provides a set of agreed models for 30 GHz, 40 Hz, and 60 GHz. Specifically, the most comprehensive one there (Model 3, originated from [54]) follows the measurements taken of practical oscillators (parameter sets A and B, for 30 GHz and 60 GHz, respectively). These parameters are summarized in Table 1.

We can utilize these models for neighboring center frequencies by shifting the response by $20 \log_{10}(f_c/f_{\text{base}})$, where f_c is the new center frequency of interest, and f_{base} is the original center frequency of the measurements (30 GHz for Set A, and 60 GHz for Set B); however, employment of these models at different frequencies is limited to a few tens of GHz away from the center frequency. Parameter sets based on practical system measurements for a frequency of interest will perform best.

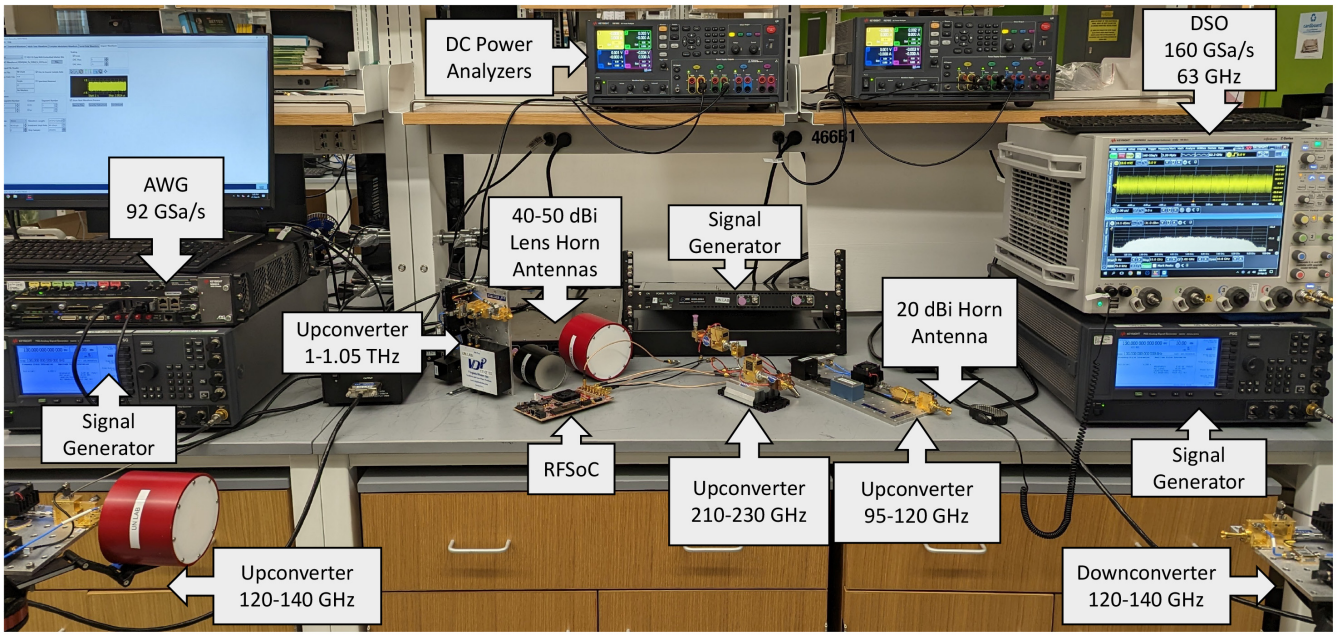

FIGURE 2. The TeraNova terahertz testbed with its various modular components.

TABLE 1. PN Model parameters (30 GHz and 60 GHz) Used in 3GPP [52], [53], [54].

	30 GHz (Set A)	60 GHz (Set B)
PSD0 (dBc/Hz)	-79.4	-70
$f_{z,n}$ (MHz)	[1.8, 2.2, 40]	[0.02, 6, 10]
$f_{p,n}$ (MHz)	[0.1, 0.2, 8]	[0.005, 0.4, 0.6]

B. MEASURING PHASE NOISE AT SUB-TERAHERTZ AND TERAHERTZ

In this section, we deliver the reference data from field measurements that are used to properly tailor the parameters of the PN model for sub-terahertz and terahertz. We also comment on the test system (our TeraNova terahertz testbed [27]) and the measurement methodology used. The high-level overview of the testbed is presented in Fig. 2.

1) HARDWARE SETUP

The TeraNova testbed transmitter consists of an analog performance signal generator (PSG) and an arbitrary waveform generator (AWG) from Keysight Technologies, different up-converter front-ends, along with directional high-gain antennas encompassing frequency ranges in the terahertz band (0.095–1.05 THz) [57]. The PSG is used to generate the LO signal and is capable of producing frequencies up to 50 GHz. The AWG is utilized to generate the intermediate frequency (IF) signal, which is mixed with the LO signal, and thus, up-converted to a higher radio frequency (RF) signal. The up-converters operate in three different frequency ranges, namely, 120–140 GHz, 210–240 GHz, and 1–1.05 THz. The 120–140 GHz up-converter front-ends consist of a frequency multiplier chain of $\times 4$, and an RF power amplifier (PA) with a gain of 20 dB. The transmit power before feeding the antenna is about 13 dBm (20 mW). The 120–140 GHz and 1–1.05 THz front-ends are all manufactured by Virginia Diodes, Inc. (VDI). The 210-240 GHz up-converter front-end has been developed in collaboration with NASA Jet Propulsion Laboratory (JPL) utilizing NASA patented frequency multiplier technology [58]. The up-converter is based on a $\times 9$ frequency multiplier chain, generating LO signals from 22.2 to 26.67 GHz to modulate the carrier with the information-bearing signal. The 1–1.05 THz up-converter front-ends have a frequency multiplier chain of $\times 24$ and similar architecture as the other VDI up-converters. It has an IF low-noise amplifier (LNA) instead of an RF PA.

The TeraNova receiver consists of a PSG and a high-performance digital storage oscilloscope (DSO) from Keysight Technologies, down-converter front-ends, along with similar high-gain antennas as the up-converters. The receiver PSG is of the same model as the transmitter PSG, and it is used to generate the LO signal at the receiver side. The DSO has a sampling rate of up to 160 GSa/s and a bandwidth of up to 63 GHz. The VDI down-converter front-ends operate in 120–140 GHz and 1–1.05 THz bands and have the same architecture as the VDI up-converter front-ends. The 210–240 GHz receiver down-converter consists of a multiplier-amplifier chain ($\times$ 6) that shifts the RF signal to the IF frequency using a mixer. In all three systems, instead of an RF PA, they utilize an IF LNA to provide the required amplification. Fig. 3 depicts how the different transmitter and receiver components are connected. The testbed has multiple sets of broadband antennas with directivity gains ranging from 21 dBi to up to 40 dBi at the aforementioned frequencies.

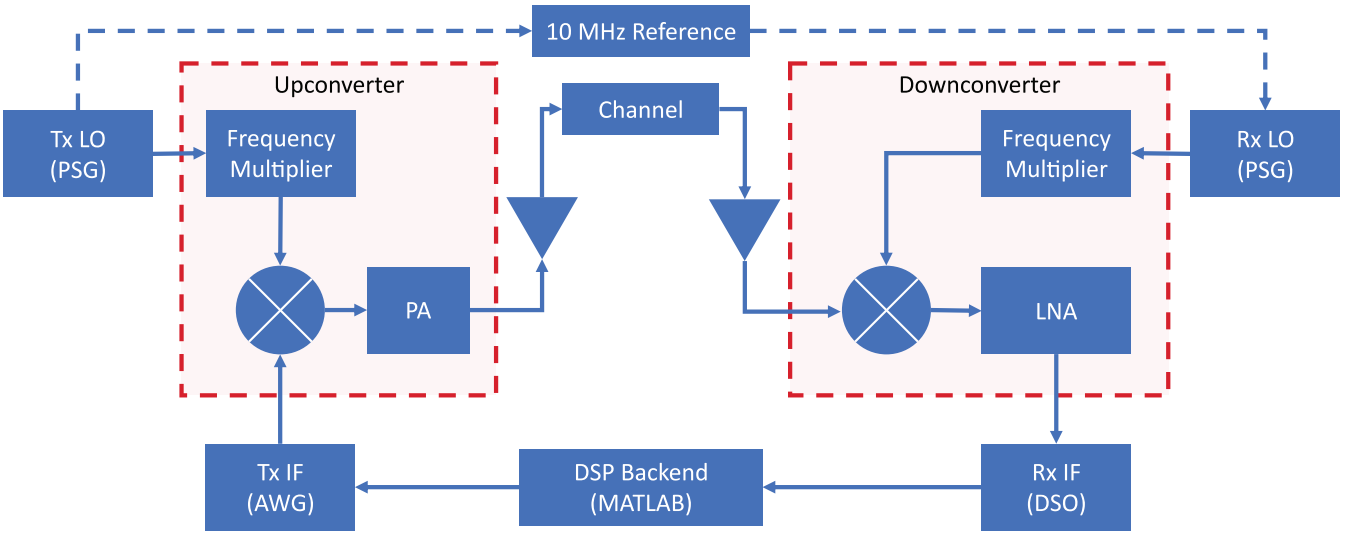

FIGURE 3. A block diagram depicting the interconnection of the various modular components of the TeraNova terahertz testbed.

2) CARRIER FREQUENCY OFFSET CONSIDERATIONS

Due to the lack of proper synchronization between the transmitter and receiver PSG internal oscillators, carrier frequency offsets (CFOs) and carrier phase offsets (CPOs) were observed during various measurements using the TeraNova testbed. The received signal at the DSO, after low-pass filtering the unwanted higher frequency components, can be written as:

$$r'(t) = A\, r(t)\, \cos\left(2\pi\, \Delta f_c t + \Delta\phi(t)\right), \tag{6}$$

where A is a constant representing an arbitrary amplitude, $r(t)$ is the intended received signal without any hardware effects/impairments, Δf_c is the CFO, and $\Delta\phi(t)$ is a stochastic process representing the total system equivalent oscillator PN. When the oscillators are not synchronized, the CFO is not zero, and thus, the observed received signal $r(t)$ at f_{IF} is distorted and is perceived as an amplitude-modulated signal with a very slow frequency equal to the CFO $\Delta f_c << f_{\text{IF}}$. The spreading around the carrier frequency is due to the effect of PN. If the CFO is zero, the received signal is only affected by PN, and it is perceived as spreading around the carrier frequency, but no amplitude modulation of the received signal is observed.

The CFO as a function of the LO frequency for the TeraNova testbed has been characterized as depicted in Fig. 4. It is shown that the CFO is in the kilohertz range, and it varies linearly with the LO frequency, having direct proportionality. The coefficient of determination of the performed linear regression was very high $R^2 = 0.9906$, which validates the linear relation between the CFO and LO frequency. The slope of the line is calculated to be about 43.32 Hz of CFO per GHz change in the LO frequency. There are several possible solutions to compensate for the CFO: (i) connect both oscillators with a 10 MHz reference cable to synchronize their clocks as shown in Fig. 3,

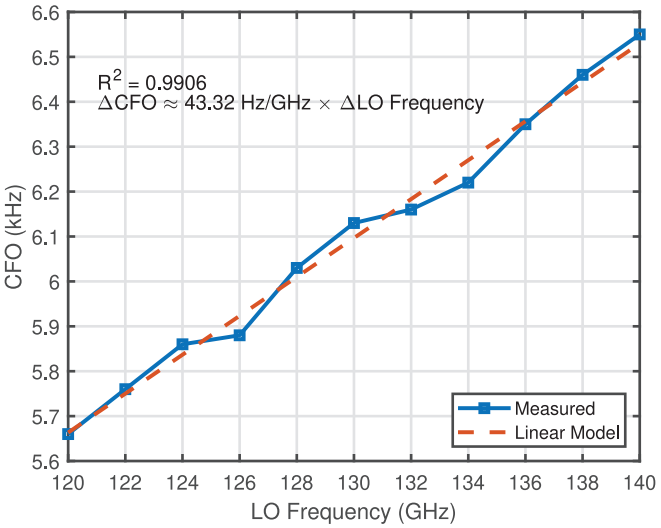

FIGURE 4. Measured carrier frequency offset as a function of the local oscillator frequency for the 120–140 GHz front-ends.

(ii) manually adjust (i.e., increase/decrease) one oscillator by the estimated CFO value in Fig. 4 according to the operating LO frequency (but the CFO can change with time due to, for example, device heating during normal operation), (iii) implement a digital phase-locked loop (PLL) to track the phase/frequency of the incoming signal and loop back to the receiver LO to adjust, or (iv) implement a digital Kalman filter tracking loop to do the same. Whenever feasible, and in all the results shown in the next sections, we use method (i). To ensure that we characterize the system PN by itself, we eliminate the CFO by connecting the transmitter and receiver oscillators with a reference 10 MHz clock. However, when performing long-range measurements, manual compensation, as explained in method (ii), can be used, as using long cables is not practical.

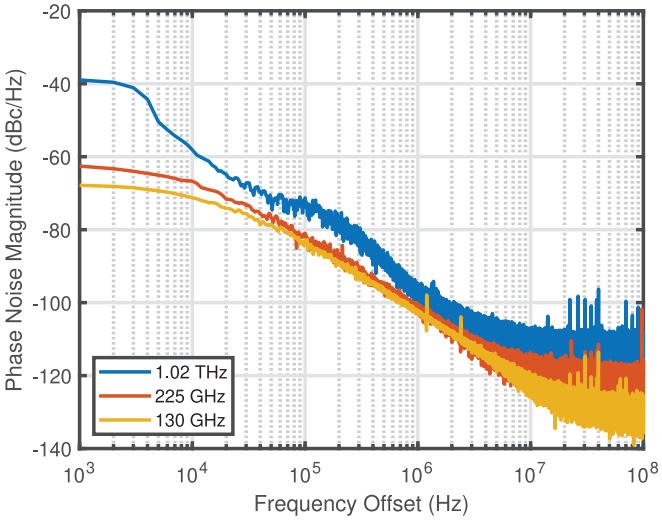

FIGURE 5. Measured single sideband PN power profile at RF frequencies 130 GHz, 225 GHz and 1.02 THz using a 5 GHz IF carrier.

3) PHASE NOISE ESTIMATION

For PN testing and measurements, a single-tone sinusoidal signal (also known as a clock signal) is sent in IF frequency using the AWG and captured back in IF via the DSO after propagating through the whole system. The captured IF signal is then post-processed in MATLAB. Particularly, we compute the power spectrum of the signal using the FFT algorithm, interpolate the spectrum using an arbitrarily small resolution bandwidth (RBW) using a piecewise cubic Hermite interpolating polynomial (PCHIP), and compute the ratio of the computed power at each offset frequency away from the carrier relative to the carrier power to obtain the single sideband (SSB) PN power profile in dBc/Hz. We repeat this process using more than 10 different consecutive captures, then average the SSB PN power profile of those captures to yield a statistically meaningful result. An example of the measured real system SSB PN power profile for the 120–140 GHz and 1–1.05 THz systems is shown in Fig. 5 using an IF tone of 5 GHz. The plots show a low overall PN power, which we anticipate from a research-grade high-performance signal generator.

C. TUNING THE 3GPP PHASE NOISE MODEL TO SUB-TERAHERTZ AND TERAHERTZ

Starting from the measured PN, we obtain new parameters to adapt the 3GPP multi-pole/zero model (5) to sub-terahertz and terahertz frequencies. Rather than a pure shift of the existing 3GPP parameters (A and B) by $20\log_{10}(f_c/f_{\text{base}})$ to our center frequencies of interest (which leads to a poor match with measurements, as in Fig. 6), our goal is to more accurately represent the PN with own parameter set. We propose additional parameter sets tuned off our measurements at 130 GHz, 225 GHz, and 1.02 THz systems in Table 2.

To derive the PN estimates, we start with choosing the 3GPP model profile, A or B, that most closely resembles

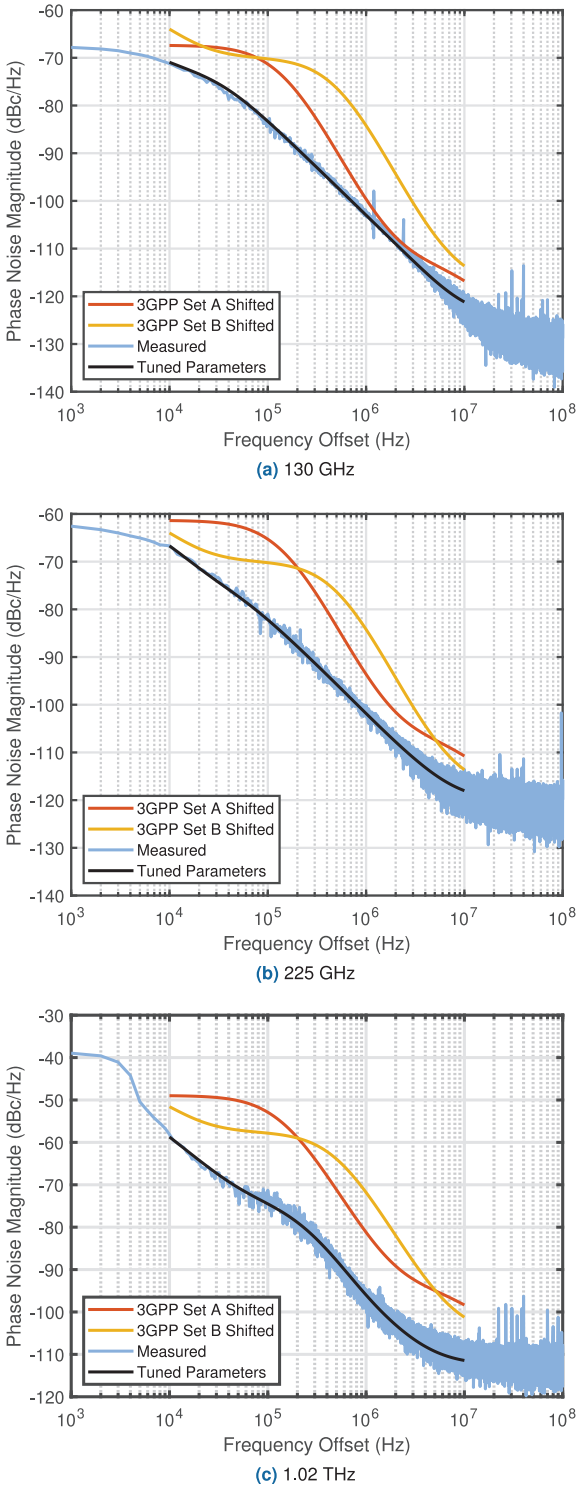

FIGURE 6. Proposed tuned PN models fit better to hardware measurements compared to 3GPP A and B extensions.

the profile of the measured values. We know f_{base} is now the frequency of the hardware system measured (130 GHz, 225 GHz, and 1.02 THz). The first zero frequency is used to adjust the overall slant of the model. The second zero is to change the slant of the higher frequency offset terms (visually on the right of the hump on the profile), and the

TABLE 2. PN Model Parameters for 130 GHz, 225 GHz, and 1.02 THz.

	130 GHz	225 GHz	1.02 THz
PSD0 (dBc/Hz)	-66.5	-60	-48
$f_{z,n}$ (MHz)	[0.01, 6, 10]	[0.03, 0.85, 8]	[0.06, 1, 5]
$f_{p,n}$ (MHz)	[0.005, 0.03, 5]	[0.005, 0.05, 0.8]	[0.003, 0.4, 0.15]

TABLE 3. Comparison of the MAPE error of the PN models.

	3GPP A	3GPP B	Our Parameters
f_c = 130 GHz	12.66%	14.10%	1.60%
f_c = 225 GHz	6.83%	8.20%	0.84%
f_c = 1.02 THz	3.17%	9.86%	0.56%

third is to edit the tail angle at the end. Then, we edit the poles to adjust the first dip with the first pole, the second dip with the second, and, lastly, readjust the finishing angle with the third pole frequency value. Multiple iterations are performed to reduce the maximum average percentage error (MAPE) and for curve fitting. MAPE gives a measure of how predictions deviate, on average, from the actual value.

Fig. 6 shows how our proposed parameters compare to the 3GPP parameter sets A and B, shifted by the appropriate $20\log_{10}(f_c/f_{\text{base}})$ correction factor for f_c of 130 GHz, 225 GHz, and 1.02 THz. We quantify the fit based in Table 3 by calculating the MAPE:

$$\text{MAPE} = \frac{100}{n}\sum_{i=1}^{n}\left|\frac{a_i - p_i}{a_i}\right|, \tag{7}$$

where n is the number of points, a_i are the actual measured values, and p_i are the modeled values. Our proposed parameters significantly improve the fit to PN observed in terahertz-band hardware.

IV. PEAK-TO-AVERAGE POWER RATIO ANALYSIS

In this section, we introduce PAPR and discuss how this metric affects the overall performance of a hardware system. With this, we incorporate PAPR limitations in our analysis by introducing a penalty based on steps taken to send signals on actual testbed equipment.

A. PAPR CALCULATION

When a signal is passed through the PA, it can become over-saturated if the amplitude exceeds a certain power threshold. Signals with random power fluctuations, or more peaks, have higher observed PAPR. Exceptionally high fluctuations can lead to signal distortion by temporarily entering the non-linear operating region of the PA. Component damage may also ensue if a signal with a high PAPR is sent with too much power. Because of this, signals with high PAPR face limited transmit power-output backoff is required to operate in the linear region, which, therefore, reduces efficiency.

For the modulation M-PSK, M-QAM, M-APSK, and DSSS schemes, we can calculate the PAPR, by computing the power for each constellation point, c_k, with

$$P(c_k) = \Re(c_k)^2 + \Im(c_k)^2, \;\; k = 0 : M-1, \tag{8}$$

and then taking the ratio of the maximum power and the average power of the set of points,

$$\text{PAPR}_{\text{dB}} = 10\log_{10}\left(\frac{\max\{P(c_k)\}}{\bar{P}(c_k)}\right), \tag{9}$$

where M is the number of constellation points. In the case of DSSS, the expected PAPR would be equal to that of the base modulation that is spread with the binary spreading sequence. For OFDM, OTFS, and DFT-s-OFDM, the calculation process is different; due to the numerous linear combinations of symbols in the IFFT operation, the number of possible outcomes is very large, so we must consider an upper bound. For OFDM, the maximum PAPR is

$$\text{PAPR}_{\text{dB}} = 10\log_{10}(N), \tag{10}$$

which is a function of the number of subcarriers, N [55]. With DFT precoding introduced in DFT-s-OFDM, this maximum PAPR is reduced–the input to the DFT block should have a relatively low PAPR, so when using the DFT followed by its inverse, the output should have PAPR properties more similar to the input [59]. With, OTFS, the PAPR grows as a function of the number of Doppler bins, rather than the subcarriers as derived in [40].

While schemes involving the use of FFT blocks tend to have a much higher PAPR, using the maximum PAPR to determine power backoff is not practical since the maximum PAPR would occur instantaneously with very low probability. To understand how reduced transmit power due to PAPR hinders performance, we propose applying a penalty that allows a direct comparison between schemes.

B. PROPOSED PAPR PENALTY

Instead of calculating the maximum PAPR for each scheme and applying a blanket signal-to-noise ratio (SNR) penalty, we propose normalizing each signal before sending it through a set noise power. Signals with higher PAPR will still get a larger penalty and we avoid the issue of over-penalizing with the low-probability maximum theoretical PAPR. We choose this practice of normalizing the signal because it is used in real hardware systems; users must re-scale the signal to fit the hardware parameters and system dynamic range, limiting the signal power. In our system (Fig. 2), we upload the signal onto the AWG, which ensures that the signal is rescaled between -1 and 1, regardless of the original signal amplitude input. This new signal is sent to the rest of the hardware and across the channel. The rescaling that occurs within the system hardware causes signals with many large peaks to get scaled significantly more than those with smaller peaks, hence, implementing a PAPR penalty [27].

We thus reuse this hardware-based PAPR consideration in our simulation study and reduce the average power

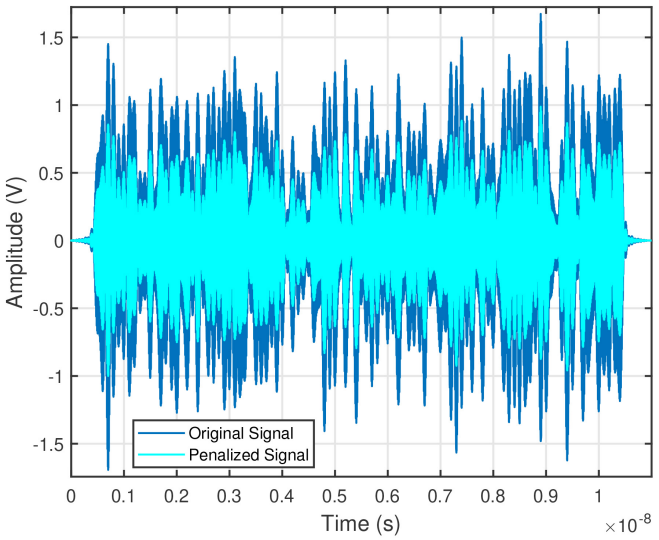

FIGURE 7. Proposed PAPR penalty applied to an example 64-QAM signal.

of the transmitted signal according to the PAPR profile of the selected modulation scheme. This reduction in the average transmit power is further referred to in the article as *"PAPR penalty"* and ensures that the maximum output signal power at any given moment does not exceed the hardware limits. One may argue that the reduction in the average power to ensure that the maximum power stays under a given level is not always needed, as some hardware components can deal with this excess themselves. However, in practical communication systems, it is preferable not to deform the transmitted signals with high peak power by simply clipping them or operating in the non-linear region of the hardware, which immediately introduces more distortion to the signal shape (and thus challenges reliable decoding at the receiver) or can even damage the hardware. Therefore, modern wireless communication systems account for the PAPR when selecting the transmit power limits in their power control. From our first-hand experience with the terahertz TearNova platform [27], certain hardware components can easily be damaged if transmitting with high output power and not accounting for non-negligible PAPR of the chosen modulation scheme.

Therefore, we incorporate this "PAPR penalty" in our analysis by rescaling the signal before sending it through the channel, essentially mimicking the hardware-centric approach. This is specifically completed by scaling the modulated signal, $s(t)$, such that

$$s(t)_{\text{penalized}} = A_{\text{sat}} \frac{s(t)}{\max |s(t)|}, \tag{11}$$

where $s(t)_{\text{penalized}}$ is the PAPR-penalized, scaled signal, and A_{sat} is the amplitude corresponding to the saturation power of the PA. Applying this uniformly among all of the signals ensures the consistency of our analysis. This procedure is further illustrated in Fig. 7 that presents a signal before and after applying the PAPR penalty.

TABLE 4. Approximate PAPR penalties applied to each scheme.

Technique	PAPR Penalty (dB)
QPSK	1.55
16-QAM	4.02
16-APSK	1.69
16-PSK	1.55
64-QAM	3.94
64-APSK	1.80
64-PSK	1.55
DSSS	1.21
DFT-s-OFDM	6.27
OFDM	12.00
OTFS	9.05

In practice, this does not affect the overall shape of the BER curve, but will instead appear to shift it towards the right. Table 4 summarizes the approximate shift, in dB, of the curve from their original performance without the penalty applied. These average values are calculated by comparing the difference between the PAPR penalized curves, and the original curves with no penalty applied.

We note that PSK modulations have a very low penalty, with the penalty mainly caused by the pulse-shaping effect on the overall PAPR. For PSK modulations, PAPR should be close to 0 dB since their constellation points have no variation in amplitude. In the amplitude-varying schemes (APSK, QAM), we see a higher penalty than PSK, with QAM always having a higher penalty for the same order. The constellation of APSK is designed to have less variation in amplitude than that of QAM, hence its lower PAPR. Beyond the base modulations, the more sophisticated schemes have a larger penalty, except DSSS, which maintains similar characteristics to its base scheme due to binary spreading. OFDM and OTFS we see a large penalty due to their use of the IFFT/FFT and ISFFT/SFFT. DFT-s-OFDM maintains a reduced penalty in comparison due to the DFT pre-processing block [55]; however, a larger penalty still exists since the DFT block size must be less than the number of subcarriers, so the effects of the FFT will not be entirely canceled out.

V. NUMERICAL RESULTS

We evaluate each modulation scheme using Monte Carlo simulations in MATLAB and show the performance for PAPR, PN, and both effects combined. Table 5 summarizes the key simulation parameters used within this numerical evaluation.

We evaluate the center frequencies corresponding with our terahertz-band hardware and PN models. We set the signal bandwidth constant to ensure a holistic comparison between schemes. For modulations such as DSSS, DFT-s-OFDM, OFDM, and OTFS which involve choosing a base modulation, we opt for QPSK for consistency as well as good performance. Parameters such as spreading

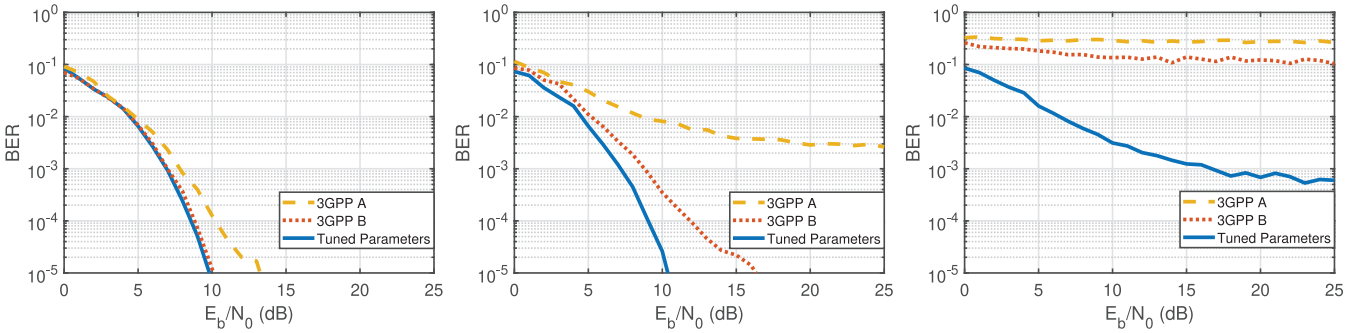

(a) f_c = 130 GHz (b) f_c = 225 GHz (c) f_c = 1.02 THz

FIGURE 8. Demonstrating the importance of accurate PN representation by showing the performance of the different models applied to QPSK.

TABLE 5. Simulation parameters.

Parameter	Value
Center Frequencies	130, 225, 1020 GHz
Signal Bandwidth	10 GHz
Base Modulations	QPSK
Spreading Factor (DSSS)	10
Subcarriers (OFDM, OTFS, DFT-s-OFDM)	128 (2 as guard)
DFT size (DFT-s-OFDM)	16
Doppler bins (OTFS)	16
Cyclic Prefix Length (OFDM, DFT-s-OFDM)	5% of symbol

factor/length, subcarriers, DFT size, and Doppler bins can influence the performance of the DSSS, OFDM, DFT-s-OFDM, and OTFS schemes. For the sake of this analysis, we chose the following set of parameters. The spreading factor is set to 10; as this number increases, the spectral efficiency is considerably reduced for minimal BER performance gain. Lower spreading factors may not capture adequately the advantages of spreading. The number of subcarriers is set to 128. Fewer subcarriers would provide better performance in the simulation, however, we would like to keep the spectral efficiency high for these techniques, so we opt to use more. The DFT size is set to less than that of the number of subcarriers, due to the requirements of DFT-s-OFDM. The Doppler bins are chosen to keep the complexity and PAPR low as higher grid sizes will influence those parameters [40], [60]. As noted earlier, a reduced cyclic prefix is best to provide performance with minimal overhead [26].

A. THE EFFECTS OF PHASE NOISE

To quantify the importance of model fit and show the effect of PN, we show the BER performance of QPSK in AWGN with the addition of PN in Fig. 8 using the PN models presented for 130 GHz, 225 GHz, and 1.02 THz. We exemplify the importance of a well-fitting model, as the results for 3GPP A and B with the adjusted center frequencies have a noticeable difference between the results with our parameters. In almost all of the cases, the 3GPP-shifted parameter set predicts significantly higher BER than the models we present. As the center frequencies extend further away from the base frequency, we see the 3GPP estimate strays further away from our parameter predictions, overestimating the PN effects. From here out, in our analysis, we use our proposed PN model parameters to demonstrate the effects of PN on the candidate modulation schemes at 130 GHz, 225 GHz, and 1.02 THz.

Fig. 9 shows the performance of all of the single-carrier schemes that we consider in the presence of the PN, given our proposed model parameters. Here we see that PN significantly impacts the overall shape of the curve. As the frequency increases, and thus, the PN profile, the performance levels off and has a high error rate. In the case of QPSK, however, the PN impact is not obvious until the 1.02 THz PN model is applied. For the other, higher-order schemes, performance degradation is immediate starting at 130 GHz. This motivates low-order mapping schemes.

In the case of DSSS, DFT-s-OFDM, OTFS, and OFDM, we chose to map to QPSK, since it is the most robust to the PN observed at terahertz frequencies. In Fig. 10 we compare the performance of these schemes in the presence of 130 GHz, 225 GHz, and 1.02 THz PN and AWGN. We see the performance of the four schemes are similar at 130 GHz, and 225 GHz, whereas at 1.02 THz, we see that OTFS and OFDM are more affected by the PN than DFT-s-OFDM and DSSS. We expect this result since multi-carrier schemes tend to have a low resistivity to PN [28]. The trend of the curve for PN at 1.02 THz changes compared to the other PN levels and reaches a BER performance asymptote. This exemplifies that PN, on its own, is significant in the terahertz band and that even when the base modulation is low-order, high PN will impose performance limitations.

B. THE EFFECTS OF PAPR

To demonstrate the effects of PAPR on performance, we start with single-carrier QPSK, 16-PSK, 16-QAM, 16-APSK, 64-PSK, 64-QAM, and 64-APSK performance in AWGN and then we factor in the penalty for PAPR, shown in Fig. 11. In general, QAM modulations tend to have higher

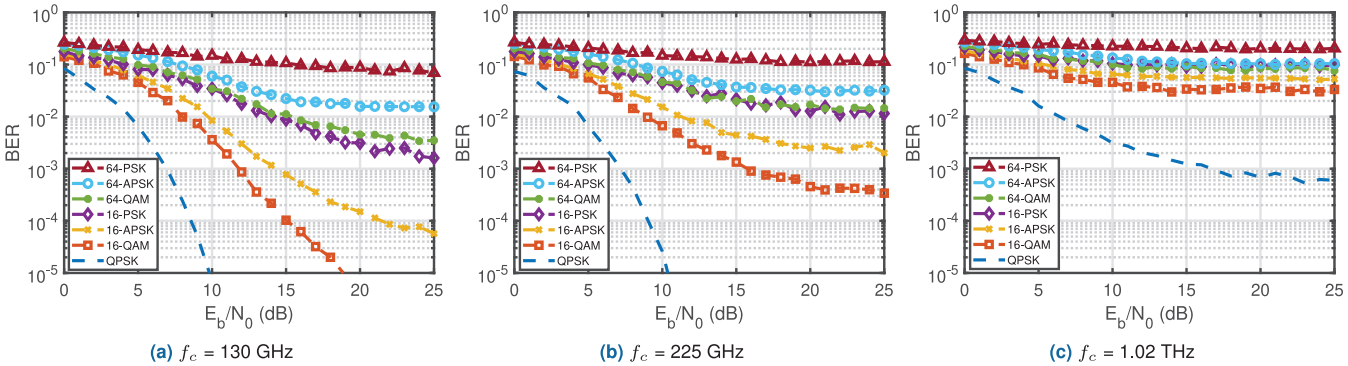

(a) f_c = 130 GHz (b) f_c = 225 GHz (c) f_c = 1.02 THz

FIGURE 9. Performance of single-carrier QPSK, 16-PSK, 16-QAM, 16-APSK, 64-PSK, 64-QAM, and 64-APSK schemes in the presence of PN, using our proposed sub-terahertz-specific and terahertz-specific model parameters for each center frequency.

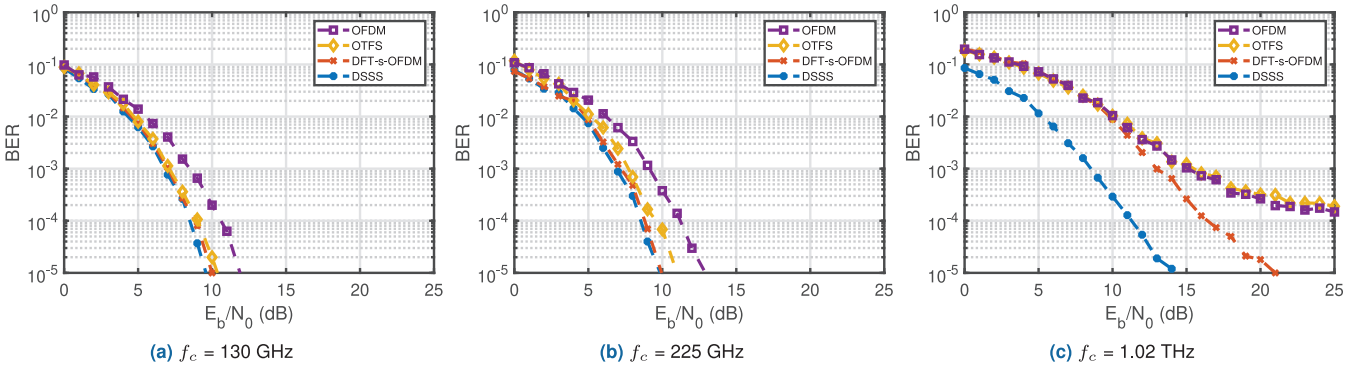

(a) f_c = 130 GHz (b) f_c = 225 GHz (c) f_c = 1.02 THz

FIGURE 10. Performance of DSSS, DFT-s-OFDM, OTFS, and OFDM with QPSK mapping in the presence of PN, using our proposed sub-terahertz-specific and terahertz-specific model parameters for each center frequency.

PAPR than their PSK or APSK counterparts of the same order, and so while theoretically, the performance should be better, when we account for PAPR by normalizing the signal before sending through the AWGN channel, the performance changes. We note that 16-APSK outperforms 16-QAM and 64-APSK outperforms 64-QAM when we adjust for the PAPR; its circular constellation shape contributes to this as there should be lower amplitude fluctuation relative to the other symbols within the constellation.

In the case of the more sophisticated schemes (DSSS, DFT-s-OFDM, OTFS, OFDM), in Fig. 12 we see that the PAPR plays a significant role in the overall performance. Considering these schemes with a QPSK base constellation, we see that initially, the performance in AWGN is very similar, but when we account for power backoff associated with the PAPR, a notable change in performance occurs. OFDM receives the most penalty followed by OTFS, DFT-s-OFDM, and DSSS. Applying the signal normalization as a PAPR penalty demonstrates that considering practical performance is crucial to accurate analysis.

C. JOINT ANALYSIS OF PHASE NOISE AND PAPR

In line with our analysis in the previous subsections, other studies have explored the effects of PN and PAPR separately. For example, in [28] and [49], the terahertz band PN levels impair the overall BER performance, and its impact is dependent on the selected modulation scheme. Simultaneously, [61], [62], [63], among others, present PAPR analysis mainly concludes that (i) PAPR is an important design consideration that ensures the equipment and signal are not deteriorated and (ii) high PAPR increases the BER, so the lower PAPR is generally preferable for reliable communications over the terahertz band. Still, these works primarily evaluate the performance as a result of one key factor (either PN or PAPR), while in real systems these impairments are combined.

Fig. 14 DSSS, DFT-s-OFDM, OFDM, and OTFS with a QPSK constellation mapping are shown in the different PN levels along with single-carrier QPSK for comparison. Here we see the primary effect influencing performance is power backoff from PAPR. We notice that the trend lines themselves follow the overall trends of QPSK in the presence of AWGN and PN, with 1.02 THz being the most obvious example of that, but the overall trend line is penalized to account for PAPR considerations.

To simulate a real system and account for both the power backoff associated with PAPR and the PN effects, we apply both to the signals and compare results. In Fig. 13 we show the performance of single-carrier QPSK, 16-PSK, 16-QAM, 16-APSK, 64-PSK, 64-QAM, and 64-APSK in the presence of 130 GHz, 225 GHz, and 1.02 THz modeled PN and accounting for PAPR.

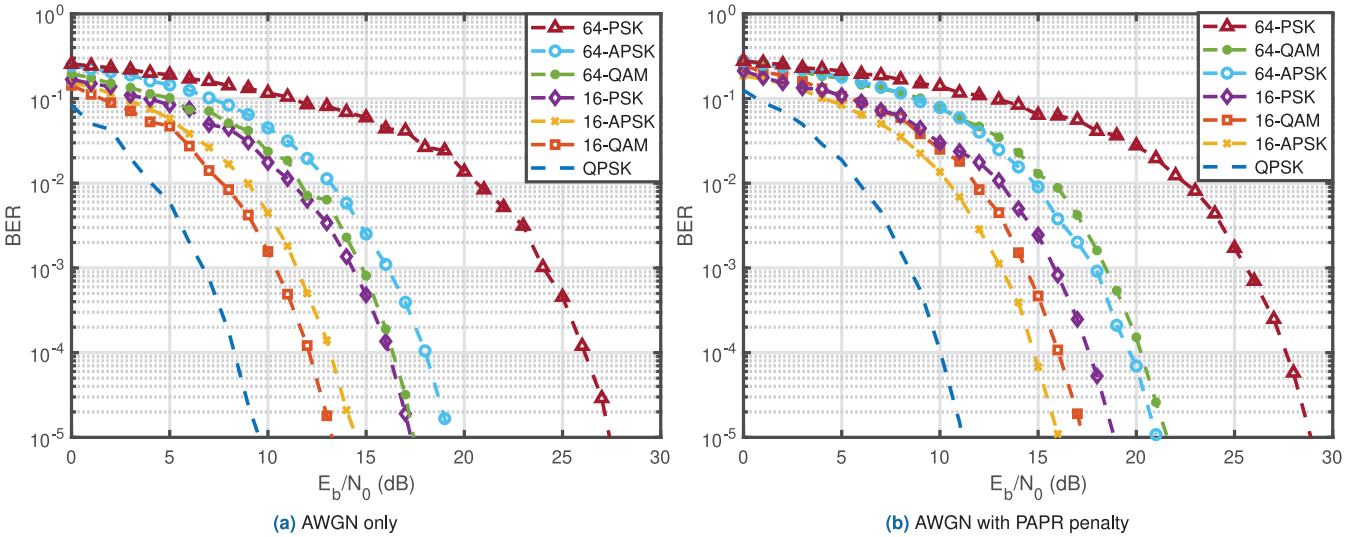

(a) AWGN only (b) AWGN with PAPR penalty

FIGURE 11. Comparison of single-carrier QPSK, 16-PSK, 16-QAM, 16-APSK, 64-PSK, 64-QAM, and 64- modulation schemes in without and with a penalty assigned for PAPR.

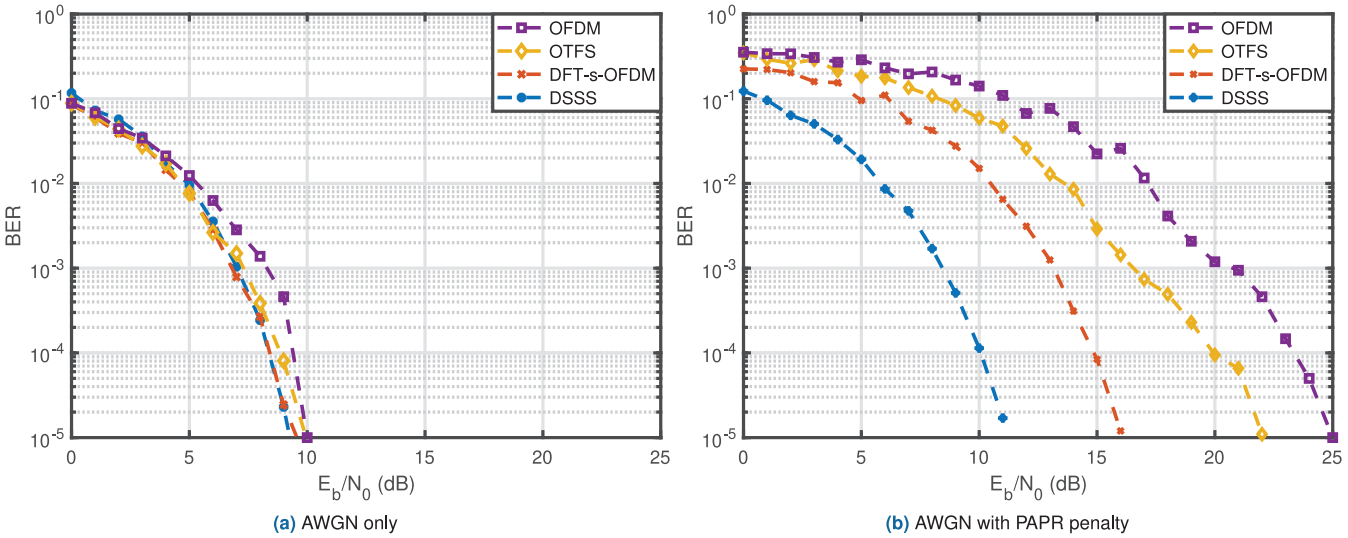

(a) AWGN only (b) AWGN with PAPR penalty

FIGURE 12. Comparison of DSSS, DFT-s-OFDM, OFDM, and OTFS with QPSK mapping in AWGN without and with a penalty assigned for PAPR.

We notice that for areas of low SNR, in the cases of 16-QAM and 16-APSK and 64-QAM and 64-APSK, the performance curves cross at about the 15 dB and 17 dB points, respectively. This exemplifies the importance of jointly evaluating both the limitations of PAPR and the effect of PN. Essentially, two regimes have been created: a low SNR and a high SNR region. For a given modulation order, in the low SNR region, we would find a scheme with better performance based on its performance in PAPR, whereas, in higher SNR scenarios, the PN factor dominates.

Since the results for the QPSK base mapping scheme follow the trend of single-carrier QPSK, as shown in Fig. 13, we can see that base modulation choice has a large impact on the overall performance of more sophisticated modulation techniques. Higher-order schemes are less robust to PN impacts, and so the selection of low-order or strategically spaced constellation points will prove to be the best base modulation choices.

While the curves show that DSSS outperforms the other schemes with respect to BER, the charts do not account for spectral efficiency. While DSSS is robust, it suffers from very low spectral efficiency, proportional to that of its spreading length. Schemes like OFDM and OTFS have better spectral efficiency but worse performance, and it is primarily due to high PAPR. Further, in the case of OFDM, inter-carrier interference due to PN increases the BER. Whereas DSSS has lower BER compared to other schemes due to low PAPR. Also, time diversity provides DSSS scheme resistance against PN at the cost of spectral efficiency. QPSK and DFT-s-OFDM fall in the middle as they possess low PAPR. Choosing the best modulation schemes for terahertz will ultimately depend on the application. For

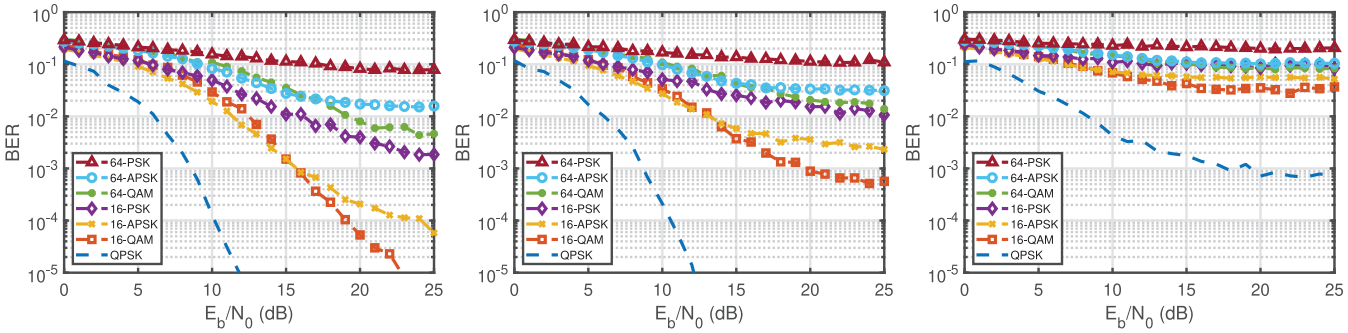

(a) PAPR penalty and 130 GHz PN (b) PAPR penalty and 225 GHz PN (c) PAPR penalty and 1.02 THz PN

FIGURE 13. Comparison of single-carrier QPSK, 16-PSK, 16-QAM, 16-APSK, 64-PSK, 64-QAM, and 64-APSK in AWGN, with PN and PAPR penalty.

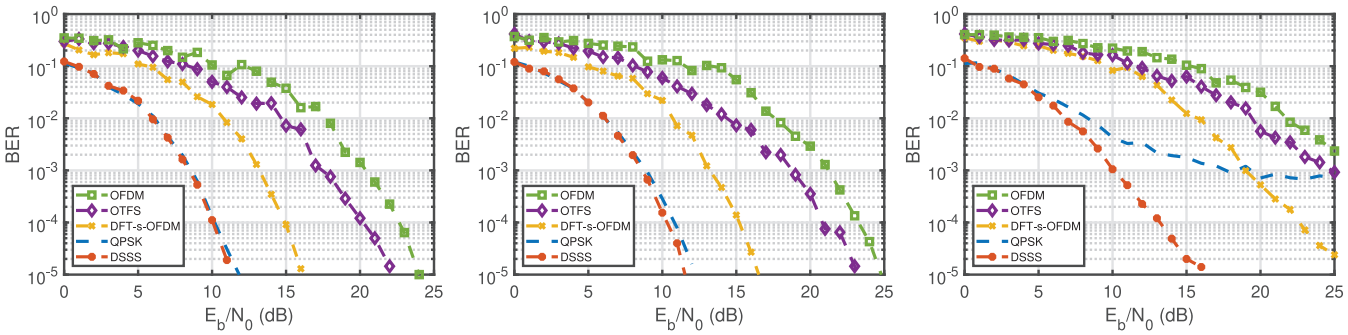

(a) PAPR penalty and 130 GHz PN (b) PAPR penalty and 225 GHz PN (c) PAPR penalty and 1.02 THz PN

FIGURE 14. Comparison of single-carrier QPSK with DSSS, DFT-s-OFDM, OFDM, and OTFS with QPSK mapping in AWGN, with PN and PAPR penalty.

scenarios that require massive amounts of data transmitted with little concern for reliability, choosing a multi-carrier scheme may make the most sense. However, restructuring of the scheme in terms of resource allocation, such as the number of sub-carriers, type of error correction, etc., is required. If reliability is more of a concern, spread spectrum could be a suitable option. For other scenarios that fall in the middle, looking towards DFT-s-OFDM or low-order pure single-carrier modulations may be the best choice.

D. SUMMARY AND POSSIBLE EXTENSIONS

Table 6 summarizes the analysis presented, providing the performance as we add each effect (AWGN, PN, PAPR, and joint) along with the spectral efficiency between schemes with the same modulation order for three SNR values (0,10,20). We note that the spectral efficiency will not exceed 2 bps/Hz for the cases compared and is calculated using the correctly received bits divided by the time and bandwidth.

Moreover, Table 6 comprehensively illustrates the effect observed in Fig. 14. For a full range of SNR setups, it is important to account for *both* the PAPR penalty and the PN-related distortions; accounting for only one of these effects leads to partial knowledge and incomplete, thus potentially incorrect, conclusions regarding the suitability of different modulation schemes. Specifically, without accounting for either of these effects, the SE of OFDM is always higher than the one of a pure QPSK. The situation changes when adding *either* the PN *or* the PAPR. Still, for SNR=10 dB, OFDM featured a *slightly higher* SE than the corresponding value for QPSK in both cases: 1.41 bps/Hz vs. 1.21 bps/Hz and 1.41 bps/Hz vs. 1.32 bps/Hz for *either* the PN *or* the PAPR.

However, the results in Table 6 change notably when accounting for *both* effects: for the same SNR of 10 dB, OFDM leads to a *lower* SE of 1.04 bps/Hz versus 1.19 for a pure QPSK and a much higher BER. This is one of the illustrative examples that these two effects *must be studied jointly (e.g., with the use of the framework developed in this article)*, while even accounting for both effects next to each other *independently* may lead to wrong conclusions when comparing the performance of different modulation schemes for sub-terahertz and terahertz communications.

Notably, both PN and PAPR impact not only the selection of the modulation and coding scheme for terahertz communications but also may have an impact on other design and performance aspects. Specifically, the consideration of the PAPR becomes crucial for the hardware design at these frequency bands as the saturation power, gain, and efficiency of PA decrease by a $\frac{1}{f_c^2}$ relation [24], hence limiting the maximum working power at the transmitter for linear mode operation of PA. Therefore, innovative solutions are required in terms of both high-power transmitter design [44] and efficient PA design to further harness the transmitter power effectively [64]. In parallel, the PN increases with the

TABLE 6. BER and SE comparison of modulation schemes for 1.02 THz: the effects of PN and PAPR independently and jointly.

Modulation ($M = 4$)	SNR (dB)	No PN, No PAPR		Only PN		Only PAPR Penalty		Both PN and PAPR Penalty	
		BER	SE (bps/Hz)	BER	SE (bps/Hz)	BER	SE (bps/Hz)	BER	SE (bps/Hz)
QPSK	0	7.87e-2	1.23	8.55e-2	1.09	1.25e-1	1.17	1.13e-1	1.03
	10	3.87e-6	1.32	3.13e-3	1.21	1.06e-4	1.32	4.29e-3	1.19
	20	<1e-6	1.33	6.82e-4	1.20	<1e-6	1.33	7.14e-4	1.20
DSSS	0	1.12e-1	0.13	8.55e-2	0.11	1.23e-1	0.12	1.42e-1	0.10
	10	4.00e-6	0.14	2.90e-4	0.12	1.14e-4	0.14	1.05e-3	0.12
	20	<1e-6	0.14	<1e-6	0.12	<1e-6	0.14	2.00e-6	0.12
OFDM	0	8.85e-2	1.48	1.96e-1	1.09	3.54e-1	1.08	4.03e-1	0.79
	10	5.12e-6	1.78	1.04e-2	1.41	1.41e-1	1.41	2.22e-1	1.04
	20	<1e-6	1.77	2.63e-4	1.75	1.19e-3	1.41	3.15e-2	1.36
DFT-s-OFDM	0	8.85e-2	1.08	3.08e-2	1.06	2.25e-1	0.92	3.52e-1	0.89
	10	5.00e-6	1.24	8.85e-3	1.32	1.51e-2	1.23	8.28e-2	1.22
	20	<1e-6	1.63	1.8e-5	1.33	<1e-6	1.52	5.28e-3	1.33
OTFS	0	8.86e-2	1.56	1.83e-1	1.13	3.47e-1	1.17	4.15e-1	0.89
	10	9.00e-6	1.89	1.03e-2	1.37	5.91e-2	1.49	1.63e-1	1.16
	20	<1e-6	1.88	3.17e-4	1.42	9.47e-5	1.87	5.64e-3	1.32

growth in the number of multipliers in the up-converter chains (to reach the designated carrier frequency starting from the LO signals). In this case, inventive solutions are required considering the generation of stable, cost-effective LO sinusoids at higher frequencies close to RF, which result in fewer multipliers being used [65].

Furthermore, in the case of fully controllable beamformers with separate up-converter chains, it is required to have robust transmission systems with low PN and efficient PN to control the multiple-input multiple-output (MIMO) encoders accurately [2], [66]. Extremely high levels of PN may even impact the radiation pattern of the terahertz phased array, potentially even leading to the shaking of the beam partially similar to the deviations caused by the beam squint effect [67], [68], [69]. Last but not least, as the presence of both PN and the PAPR increase the BER, forward error correcting codes such as low-density parity-check (LDPC) [47] or low-weight error prevention code (EPC) [70] are essential for error-free transmission over the terahertz band channel. All these considerations confirm the importance of carefully characterizing both the PN and the PAPR characteristics of prospective terahertz communication systems. Here, our delivered framework and results may be utilized further for other terahertz-related research activities beyond the selection of the most suitable modulation and coding scheme.

VI. CONCLUSION

In this paper, we present a comprehensive analysis of candidate modulation techniques for terahertz-band communications *in the joint presence of two key practical systems limitations, namely PN and PAPR*. We contribute a set of model parameters based on system measurements for PN at 130 GHz, 225 GHz, and 1.02 THz as well as a method to simulate the detriment of PAPR on signal performance. We finally conduct an extensive numerical analysis to understand the interplay between these effects and their joint impact on the performance of the (sub-)terahertz and terahertz communication systems.

From our results, we find that low-order modulation schemes will perform best in the conditions of current sub-terahertz and terahertz hardware. DSSS is very robust in the presence of both PAPR and PN but lacks spectral efficiency compared to other schemes. DFT-s-OFDM is also a robust solution with better spectral efficiency but can be outperformed by basic single-carrier modulation like QPSK at lower SNR. OTFS and OFDM, while spectrally efficient, tend to suffer more from the terahertz hardware effects. Hence, as we observe, in practical implementations, the choice of modulation is likely to be application- and scenario-dependent.

This work facilitates a more informed selection here by providing both the comprehensive evaluation methodology with two key aspects of the terahertz hardware accounted for and the initial set of illustrative numerical results highlighting the essential trade-offs between the compared modulation solutions for prospective 6G and beyond terahertz wireless communication systems. Importantly, certain elements of the presented methodology (e.g., the developed PN models and the calculated PAPR penalty coefficients) can be reused in further studies on terahertz wireless systems, when exploring the joint effect of PN and PAPR on beamforming solutions or the design of the terahertz hardware components, among other essential aspects.

ACKNOWLEDGMENT

The authors would like to thank Duschia Bodet for her invaluable technical feedback. Approved for Public Release; Distribution Unlimited: AFRL-2023-6127.

REFERENCES

[1] C. Han et al., "Terahertz wireless channels: A holistic survey on measurement, modeling, and analysis," *IEEE Commun. Surveys Tuts.*, vol. 24, no. 3, pp. 1670–1707, 3rd Quart., 2022.

[2] B. Ning et al., "Beamforming technologies for ultra-massive MIMO in terahertz communications," *IEEE Open J. Commun. Soc.*, vol. 4, pp. 614–658, 2023.

[3] H.-J. Song and N. Lee, "Terahertz communications: Challenges in the next decade," *IEEE Trans. THz Sci. Technol.*, vol. 12, no. 2, pp. 105–117, Mar. 2022.

[4] H. Jiang, M. Mukherjee, J. Zhou, and J. Lloret, "Channel modeling and characteristics for 6G wireless communications," *IEEE Netw.*, vol. 35, no. 1, pp. 296–303, Jan./Feb. 2021.

[5] H. Elayan, O. Amin, B. Shihada, R. M. Shubair, and M.-S. Alouini, "Terahertz band: The last piece of RF spectrum puzzle for communication systems," *IEEE Open J. Commun. Soc.*, vol. 1, pp. 1–32, 2020.

[6] K. Tekbıyık, A. R. Ekti, G. K. Kurt, and A. Görçin, "Terahertz band communication systems: Challenges, novelties and standardization efforts," *Phys. Commun.*, vol. 35, Aug. 2019, Art. no. 100700.

[7] H. Jiang et al., "Novel statistical wideband MIMO V2V channel modeling using unitary matrix transformation algorithm," *IEEE Trans. Wireless Commun.*, vol. 20, no. 8, pp. 4947–4961, Aug. 2021.

[8] T. S. Rappaport et al., "Wireless communications and applications above 100 GHz: Opportunities and challenges for 6G and beyond," *IEEE Access*, vol. 7, pp. 78729–78757, 2019.

[9] K. Guan et al., "Towards realistic high-speed train channels at 5G millimeter-wave band—Part I: Paradigm, significance analysis, and scenario reconstruction," *IEEE Trans. Veh. Technol.*, vol. 67, no. 10, pp. 9112–9128, Oct. 2018.

[10] K. Guan et al., "Towards realistic high-speed train channels at 5G millimeter-wave band—Part II: Case study for paradigm implementation," *IEEE Trans. Veh. Technol.*, vol. 67, no. 10, pp. 9129–9144, Oct. 2018.

[11] D. He et al., "Physics and AI-based digital twin of multi-spectrum propagation characteristics for communication and sensing in 6G and beyond," *IEEE J. Sel. Areas Commun.*, vol. 41, no. 11, pp. 3461–3473, Nov. 2023.

[12] S. Ju, Y. Xing, O. Kanhere, and T. S. Rappaport, "Millimeter wave and sub-Terahertz spatial statistical channel model for an indoor office building," *IEEE J. Sel. Areas Commun.*, vol. 39, no. 6, pp. 1561–1575, Jun. 2021.

[13] K. Guan, H. Yi, D. He, B. Ai, and Z. Zhong, "Towards 6G: Paradigm of realistic terahertz channel modeling," *China Commun.*, vol. 18, no. 5, pp. 1–18, May 2021.

[14] Y. Chen, Y. Li, C. Han, Z. Yu, and G. Wang, "Channel measurement and ray-tracing-statistical hybrid modeling for low-Terahertz indoor communications," *IEEE Trans. Wireless Commun.*, vol. 20, no. 12, pp. 8163–8176, Dec. 2021.

[15] Y. Yan, X. Gao, and J. An, "Joint multipath-shadow-weather fading channel modeling for Terahertz wireless communication," in *Proc. Int. Conf. Microw. Millimeter Wave Technol. (ICMMT)*, 2023, pp. 1–3.

[16] N. A. Abbasi et al., "Double-directional channel measurements for urban THz microcellular communications in a street canyon," in *Proc. IEEE Int. Conf. Commun.*, May 2022, pp. 2876–2881.

[17] J. M. Eckhardt, V. Petrov, D. Moltchanov, Y. Koucheryavy, and T. Kürner, "Channel measurements and modeling for low-Terahertz band vehicular communications," *IEEE J. Sel. Areas Commun.*, vol. 39, no. 6, pp. 1590–1603, Jun. 2021.

[18] Y. Xing and T. S. Rappaport, "Propagation measurements and path loss models for sub-THz in urban microcells," in *Proc. IEEE Int. Conf. Commun. (ICC)*, Jun. 2021, pp. 1–6.

[19] Ö. T. Demir and E. Björnson, "Channel estimation in massive MIMO under hardware non-linearities: Bayesian methods versus deep learning," *IEEE Open J. Commun. Soc.*, vol. 1, pp. 109–124, 2020.

[20] Y. Wu, Y. Gu, and Z. Wang, "Efficient channel estimation for mmWave MIMO with transceiver hardware impairments," *IEEE Trans. Veh. Technol.*, vol. 68, no. 10, pp. 9883–9895, Oct. 2019.

[21] S. Choi and E.-R. Jeong, "Digital predistortion based on combined feedback in MIMO transmitters," *IEEE Commun. Lett.*, vol. 16, no. 10, pp. 1572–1575, Oct. 2012.

[22] A. C. M. Austin, O. Afisiadis, and A. Burg, "Digital predistortion of hardware impairments for full-duplex transceivers," in *Proc. IEEE Glob. Conf. Signal Inf. Process. (GlobalSIP)*, Nov. 2017, pp. 878–882.

[23] S. Bicaïs, J.-B. Doré, G. Gougéon, and Y. Corre, "Optimized single carrier transceiver for future sub-TeraHertz applications," in *Proc. IEEE Int. Conf. Acoust. Speech Signal Process. (ICASSP)*, May 2020, pp. 5095–5099.

[24] H. Wang et al. "Power amplifiers performance survey 2000-present." Nov. 2020. [Online]. Available: https://gems.ece.gatech.edu/PA_survey.html

[25] I. F. Akyildiz, C. Han, Z. Hu, S. Nie, and J. M. Jornet, "Terahertz band communication: An old problem revisited and research directions for the next decade," *IEEE Trans. Commun.*, vol. 70, no. 6, pp. 4250–4285, Jun. 2022.

[26] S. Chakraborty, C. Parisi, D. Saha, and N. Thawdar, "A case for OFDM in ultra-broadband Terahertz communication: An experimental approach," in *Proc. 5th ACM Workshop Millimeter-Wave Terahertz Netw. Sens. Syst.*, Oct. 2021, pp. 1–6.

[27] P. Sen, D. A. Pados, S. N. Batalama, E. Einarsson, J. P. Bird, and J. M. Jornet, "The TeraNova platform: An integrated testbed for ultra-broadband wireless communications at true Terahertz frequencies," *Comput. Netw.*, vol. 179, Oct. 2020, Art. no. 107370.

[28] S. Tarboush, H. Sarieddeen, M.-S. Alouini, and T. Y. Al-Naffouri, "Single- versus multicarrier Terahertz-band communications: A comparative study," *IEEE Open J. Commun. Soc.*, vol. 3, pp. 1466–1486, 2022.

[29] H. G. Myung, "Introduction to single carrier FDMA," in *Proc. 15th Eur. Signal Process. Conf.*, Sep. 2007, pp. 2144–2148.

[30] G. Berardinelli, K. I. Pedersen, T. B. Sorensen, and P. Mogensen, "Generalized DFT-spread-OFDM as 5G waveform," *IEEE Commun. Mag.*, vol. 54, no. 11, pp. 99–105, Nov. 2016.

[31] G. Berardinelli, F. M. L. Tavares, T. B. Sørensen, P. Mogensen, and K. Pajukoski, "On the potential of zero-tail DFT-spread-OFDM in 5G networks," in *Proc. IEEE 80th Veh. Technol. Conf. (VTC-Fall)*, Sep. 2014, pp. 1–6.

[32] M. Nemati, H. Takshi, and H. Arslan, "Discrete fourier transform spread zero word OFDM," in *Proc. IEEE Int. Black Sea Conf. Commun. Netw. (BlackSeaCom)*, Jun. 2017, pp. 1–5.

[33] Y. Xin, T. Bao, J. Hua, and G. Yu, "A novel waveform scheme for THz communications," in *Proc. IEEE 94th Veh. Technol. Conf. (VTC2021-Fall)*, Sep. 2021, pp. 1–6.

[34] U. Kumar, C. Ibars, A. Bhorkar, and H. Jung, "A waveform for 5G: Guard interval DFT-s-OFDM," in *Proc. IEEE Globecom Workshops (GC Wkshps)*, Dec. 2015, pp. 1–6.

[35] M. Nemati, H. Takshi, and H. Arslan, "A flexible hybrid waveform," in *Proc. IEEE Int. Black Sea Conf. Commun. Netw. (BlackSeaCom)*, Jun. 2017, pp. 1–5.

[36] Y. Wu, C. Han, and T. Yang, "DFT-spread orthogonal time frequency space modulation design for Terahertz communications," in *Proc. IEEE Glob. Commun. Conf. (GLOBECOM)*, Dec. 2021, pp. 1–6.

[37] Y. Wu, C. Han, and Z. Chen, "DFT-spread orthogonal time frequency space system with superimposed pilots for Terahertz integrated sensing and communication," *IEEE Trans. Wireless Commun.*, vol. 22, no. 11, pp. 7361–7376, Nov. 2023.

[38] R. Hadani and A. Monk, "OTFS: A new generation of modulation addressing the challenges of 5G," Feb. 2018, *arXiv:1802.02623*.

[39] M. Ramachandran, G. Surabhi, and A. Chockalingam, "OTFS: A new modulation scheme for high-mobility use cases," *J. Indian Inst. Sci.*, vol. 100, pp. 315–336, Apr. 2020.

[40] G. D. Surabhi, R. M. Augustine, and A. Chockalingam, "Peak-to-average power ratio of OTFS modulation," *IEEE Commun. Lett.*, vol. 23, no. 6, pp. 999–1002, Jun. 2019.

[41] T. S. Rappaport and J. C. Liberti, *Smart Antennas for Wireless CDMA*. Piscataway, NJ, USA: IEEE Press, Jan. 1999.

[42] C. Bosso, P. Sen, X. Cantos-Roman, C. Parisi, N. Thawdar, and J. M. Jornet, "Ultrabroadband spread spectrum techniques for secure dynamic spectrum sharing above 100 GHz between active and passive users," in *Proc. IEEE Int. Symp. Dyn. Spectr. Access Netw. (DySPAN)*, Dec. 2021, pp. 45–52.

[43] P. Sen, H. Pandey, and J. M. Jornet, "Ultra-broadband chirp spread spectrum communication in the terahertz band," in *Next-Gener. Spectrosc. Technol. XIII*, L. T. Profeta, A. K. Azad, and S. M. Barnett, Eds., vol. 11390. Bellingham, WA, USA: SPIE, May 2020, Art. no. 113900G.

[44] P. Sen, J. V. Siles, N. Thawdar, and J. M. Jornet, "Multi-kilometre and multi-gigabit-per-second sub-terahertz communications for wireless backhaul applications," *Nat. Electron.*, vol. 6, no. 2, pp. 164–175, 2023.

[45] M. F. Hermelo, P.-T. B. Shih, M. Steeg, A. Ng'oma, and A. Stöhr, "Spectral efficient 64-QAM-OFDM terahertz communication link," *Opt. Exp.*, vol. 25, no. 16, pp. 19360–19370, Aug. 2017.

[46] P. Sen, V. Ariyarathna, and J. M. Jornet, "An optimized M-ary amplitude phase shift keying scheme for ultrabroadband Terahertz communication," in *Proc. IEEE 19th Annu. Consum. Commun. Netw. Conf. (CCNC)*, Jan. 2022, pp. 661–666.

[47] V. Petrov, T. Kurner, and I. Hosako, "IEEE 802.15.3d: First standardization efforts for sub-Terahertz band communications toward 6G," *IEEE Commun. Mag.*, vol. 58, no. 11, pp. 28–33, Nov. 2020.

[48] D. Bodet, P. Sen, Z. Hossain, N. Thawdar, and J. M. Jornet, "Hierarchical bandwidth modulations for ultra-broadband communications in the Terahertz band," *IEEE Trans. Wireless Commun.*, vol. 22, no. 3, pp. 1931–1947, Mar. 2023.

[49] P. Desombre, H. Farès, and Y. Louët, "Performance comparison of digital modulations in the presence of Gaussian phase noise in the sub-THz context," in *Proc. 4th Int. Workshop Mobile Terahertz Syst. (IWMTS)*, Jul. 2021, pp. 1–5.

[50] M. Jian and R. Liu, "Baseband signal processing for Terahertz: Waveform design, modulation and coding," in *Proc. Int. Wireless Commun. Mobile Comput. (IWCMC)*, Jun. 2021, pp. 1710–1715.

[51] C. Han, Y. Wu, Z. Chen, Y. Chen, and G. Wang, "THz ISAC: A physical-layer perspective of Terahertz integrated sensing and communication," Jan. 2023, *arxiv-2209.03145*.

[52] "Study on new radio access technology physical layer aspects," 3GPP, Sophia Antipolis, France, 3GPP Rep. TR 38.802 V14.2.0, Sep. 2017.

[53] "WF on phase noise modeling (document for decision, WG1 #85, agenda item: 7.1.2)," 3GPP, Sophia Antipolis, France, 3GPP Rep. R1–165685, May 2016.

[54] "Samsung, discussion on phase noise modeling," 3GPP, Sophia Antipolis, France, 3GPP Rep. R1–163984, May 2016.

[55] H. Asplund et al., "Chapter 5 - OFDM-based MIMO systems," in *Advanced Antenna Systems for 5G Network Deployments*, H. Asplund et al., Eds. Cambridge, MA, USA: Academic Press, Jul. 2020, pp. 133–174.

[56] Y. Hong, T. Thaj, and E. Viterbo, "Chapter 4 - delay-doppler modulation," in *Delay-Doppler Communications*, Y. Hong, T. Thaj, and E. Viterbo, Eds. Cambridge, MA, USA: Academic Press, Mar. 2022, pp. 47–91.

[57] P. Sen, V. Ariyarathna, A. Madanayake, and J. M. Jornet, "A versatile experimental testbed for ultrabroadband communication networks above 100 GHz," *Comput. Netw.*, vol. 193, Jul. 2021, Art. no. 108092.

[58] I. Mehdi, J. V. Siles, C. Lee, and E. Schlecht, "THz diode technology: Status, prospects, and applications," *Proc. IEEE*, vol. 105, no. 6, pp. 990–1007, Jun. 2017.

[59] W. Shieh and I. Djordjevic, "Chapter 2-OFDM principles," in *OFDM for Optical Communications*, W. Shieh and I. Djordjevic, Eds. Oxford, U.K.: Academic Press, Mar. 2010, pp. 31–52.

[60] T. M. C. Chu, H.-J. Zepernick, A. Westerhagen, A. Höök, and B. Granbom, "Performance assessment of OTFS modulation in high doppler airborne communication networks," *Mobile Netw. Appl.*, vol. 27, no. 4, pp. 1746–1756, Aug. 2022.

[61] V. K. Padarti, C. Dasari, P. V. Venu Gopal Dokala, V. Sravya Chowtapalli, and L. V. R. Kowshik Avula, "An efficient clipping method for PAPR reduction in OFDM systems," in *Proc. Int. Conf. Invent. Comput. Technol. (ICICT)*, 2022, pp. 624–629.

[62] H. Wang and X. Chen, "Measurement of OFDM signals with PAPR reduction in the presence of hardware impairments," in *Proc. IEEE MTT-S Int. Conf. Numer. Electromagn. Multiphys. Model. Optim. (NEMO)*, 2020, pp. 1–4.

[63] P. J. Green, "Peak-to-average power ratio and power amplifier backoff requirements in wireless transmissions," in *Proc. IEEE Region 10 Conf. (TENCON)*, 2017, pp. 630–633.

[64] J. C. Tucek, M. A. Basten, D. A. Gallagher, and K. E. Kreischer, "Operation of a compact 1.03 THz power amplifier," in *Proc. IEEE Int. Vacuum Electron. Conf. (IVEC)*, 2016, pp. 1–2.

[65] T. D. Nguyen and J.-P. Hong, "A high fundamental frequency sub-THz CMOS oscillator with a capacitive load reduction circuit," *IEEE Trans. Microw. Theory Techn.*, vol. 68, no. 7, pp. 2655–2667, Jul. 2020.

[66] D. Headland, Y. Monnai, D. Abbott, C. Fumeaux, and W. Withayachumnankul, "Tutorial: Terahertz beamforming, from concepts to realizations," *APL Photon.*, vol. 3, no. 5, 2018, Art. no. 51101.

[67] C. Han, L. Yan, and J. Yuan, "Hybrid beamforming for Terahertz wireless communications: Challenges, architectures, and open problems," *IEEE Wireless Commun.*, vol. 28, no. 4, pp. 198–204, Aug. 2021.

[68] N. T. Nguyen, J. Kokkoniemi, and M. Juntti, "Beam squint effects in THz communications with UPA and ULA: Comparison and hybrid beamforming design," in *Proc. IEEE Globecom Workshops (GC Wkshps)*, Dec. 2022, pp. 1754–1759.

[69] B. Chatelier and M. Crussière, "On the impact of phase noise on beamforming performance for mmWave massive MIMO systems," in *Proc. IEEE Wireless Commun. Netw. Conf. (WCNC)*, 2022, pp. 1563–1568.

[70] J. M. Jornet and I. F. Akyildiz, "Low-weight channel coding for interference mitigation in electromagnetic Nanonetworks in the Terahertz band," in *Proc. IEEE Int. Conf. Commun. (ICC)*, 2011, pp. 1–6.

CLAIRE T. PARISI (Member, IEEE) received the B.S. degree in electrical engineering from Clarkson University, Potsdam, NY, USA, in 2020, and the M.S. degree in electrical and computer engineering from Northeastern University, Boston, MA, USA, in 2022. She is an Electronics Engineer with the AFRL–Information Directorate, Rome, NY, USA. She has been with AFRL since 2019, conducting research on terahertz band communications. Her current research interests include wireless communications in the millimeter-wave and terahertz bands, modulations and waveforms for next-generation communications, and machine learning.

SHERIF BADRAN (Graduate Student Member, IEEE) received the B.S. degree in electrical, electronics and communications engineering from the Faculty of Engineering, Ain Shams University, Cairo, Egypt, in 2021, and the M.S. degree in electrical and computer engineering from Northeastern University, Boston, MA, USA, in 2023, where he is currently pursuing the Ph.D. degree in electrical engineering with the Department of Electrical and Computer Engineering under the guidance of Dr. J. M. Jornet in the Ultrabroadband Nanonetworking Laboratory and a Graduate Research Assistant. His current research interests include digital and statistical signal processing for terahertz communications, experimentation and characterization of terahertz wireless systems, and coding theory.

PRIYANGSHU SEN (Member, IEEE) received the Bachelor of Technology degree from the Biju Patnaik University of Technology, India, in 2012, the Master of Technology degree in radio physics and electronics from the University of Calcutta, India, in 2015, and the Ph.D. degree from the Department of Electrical and Computer Engineering, Northeastern University, Boston, MA, USA, in 2022, under the guidance of Professor J. M. Jornet in the Ultrabroadband Nanonetworking Laboratory, Boston. He completed his industrial training in Garden Reach Shipbuilders and Engineers Ltd. on the communication system on a naval board ship, in 2011. He started his career as a Research Engineer of Radio Physics and Electronics with the University of Calcutta in 2013. He completed his summer training at Samsung Research America in the sub-terahertz communication system and protocol design in 2019. He is an Assistant Professor with the Department of Engineering, SUNY Polytechnic Institute. His current research interests include experimental and statistical characterization of terahertz communication channels and networks.

VITALY PETROV (Member, IEEE) received the M.Sc. degree in information systems security from SUAI University, St. Petersburg, Russia, in 2011, the M.Sc. degree in IT and communications engineering from the Tampere University of Technology, Tampere, Finland, in 2014, and the Ph.D. degree in communications engineering from Tampere University, Finland, in 2020. He is a Principal Research Scientist with Northeastern University, Boston, MA, USA. Before joining Northeastern University in 2022, he was a Senior Standardization Specialist and a 3GPP RAN1 delegate with Nokia Bell Labs and later Nokia Standards. During the Ph.D. studies, he was a Visiting Researcher with the University of Texas at Austin, the Georgia Institute of Technology, and King's College London. His current research interests include terahertz band communications and networking. He is a recipient of the Best Student Paper Award at IEEE VTC-Fall 2015, the Best Student Poster Award at IEEE WCNC 2017, and the Best Student Journal Paper Award from IEEE Finland in 2019.

JOSEP MIQUEL JORNET (Fellow, IEEE) received the degree in telecommunication engineering and the Master of Science degree in information and communication technologies from the Universitat Politècnica de Catalunya, Spain, in 2008, and the Ph.D. degree in electrical and computer engineering from the Georgia Institute of Technology, Atlanta, GA, USA, in August 2013. He is a Professor with the Department of Electrical and Computer Engineering, the Director of the Ultrabroadband Nanonetworking Laboratory, and the Associate Director of the Institute for the Wireless Internet of Things, Northeastern University. Between August 2013 and August 2019, he was with the Department of Electrical Engineering, University at Buffalo, The State University of New York. He is a leading expert in terahertz communications, in addition to wireless nano-bio-communication networks and the Internet of Nano-Things. In these areas, he has coauthored more than 240 peer-reviewed scientific publications, including one book, and has been granted five U.S. patents. His work has received over 15 500 citations (H-index of 56 as of September 2023). He is serving as the lead PI on multiple grants from U.S. federal agencies, including the National Science Foundation, the Air Force Office of Scientific Research, and the Air Force Research Laboratory as well as industry. He is the recipient of multiple awards, including the 2017 IEEE ComSoc Young Professional Best Innovation Award, the 2017 ACM NanoCom Outstanding Milestone Award, the NSF CAREER Award in 2019, the 2022 IEEE ComSoc RCC Early Achievement Award, and the 2022 IEEE Wireless Communications Technical Committee Outstanding Young Researcher Award, among others, as well as four best paper awards. He is an IEEE ComSoc Distinguished Lecturer from 2022 to 2023. He is also the Editor-in-Chief of the *Nano Communication Networks* (Elsevier) and an Editor of IEEE TRANSACTIONS ON COMMUNICATIONS.